

Probable detection of **an eruptive filament** from a super-flare on a solar-type star

Kosuke Namekata^{1,2,3*}, Hiroyuki Maehara⁴, Satoshi Honda⁵, Yuta Notsu^{6,7,8}, Soshi Okamoto¹, Jun Takahashi⁵, Masaki Takayama⁵, Tomohito Ohshima⁵, Tomoki Saito⁵, Noriyuki Katoh^{5,9}, Miyako Tozuka⁵, Katsuhiro L. Murata¹⁰, Futa Ogawa¹⁰, Masafumi Niwano¹⁰, Ryo Adachi¹⁰, Motoki Oeda¹⁰, Kazuki Shiraishi¹⁰, Keisuke Isogai^{2,11}, Daikichi, Seki^{1,2,12}, Takako T. Ishii², Kiyoshi Ichimoto², Daisaku Nogami¹ & Kazunari Shibata^{13,14}

¹*Department of Astronomy, Kyoto University, Sakyo, Kyoto, Japan*

²*Astronomical Observatory, Kyoto University, Sakyo, Kyoto, Japan*

³*ALMA Project, NAOJ, NINS, Osawa, Mitaka, Tokyo, Japan*

⁴*Okayama Branch Office, Subaru Telescope, National Astronomical Observatory of Japan, NINS, Asakuchi, Okayama, Japan*

⁵*Nishi-Harima Astronomical Observatory, Center for Astronomy, University of Hyogo, Sayo, Hyogo, Japan*

⁶*Laboratory for Atmospheric and Space Physics, University of Colorado Boulder, Boulder, CO, USA*

⁷*National Solar Observatory, Boulder, CO, USA*

⁸*Department of Earth and Planetary Sciences, Tokyo Institute of Technology, Meguro, Tokyo, Japan*

⁹*Graduate School of Human Development and Environment, Kobe University, Nada, Kobe, Japan*

¹⁰*Department of Physics, Tokyo Institute of Technology, Meguro, Tokyo, Japan*

¹¹*Department of Multi-Disciplinary Sciences, Graduate School of Arts and Sciences, The University of Tokyo, Meguro, Tokyo, Japan*

¹²*Graduate School of Advanced Integrated Studies in Human Survivability, Kyoto University, Sakyo, Kyoto, Japan*

¹³*Kwasan Observatory, Kyoto University, Yamashina, Kyoto, Japan*

¹⁴*School of Science and Engineering, Doshisha University, Kyotanabe, Kyoto, Japan*

Solar flares are often accompanied by filament/prominence eruptions ($\sim 10^4$ K and $\sim 10^{10-11}$ cm⁻³), sometimes leading to **coronal mass ejections (CMEs)** that directly affect the Earth's environment^{1,2}. **'Superflares'** are found on some active solar-type (G-type main-sequence) stars³⁻⁵, but the association of filament eruptions/CMEs has not been established. Here we show that our optical spectroscopic observation of the young solar-type star EK Draconis reveals the evidence for a stellar filament eruption associated with a superflare. This superflare emitted a radiated energy of 2.0×10^{33} erg, and blue-shifted hydrogen absorption component with a large velocity of -510 km s⁻¹ was observed shortly after. The temporal changes in the spectra greatly resemble those of solar filament eruptions. Comparing this eruption with solar filament eruptions in terms of the length scale and velocity strongly suggests that a stellar CME occurred. The erupted filament mass of 1.1×10^{18} g is 10 times larger than those of the largest solar CMEs. The massive filament eruption and an associated CME provide the opportunity to evaluate how they affect the environment of young exoplanets/young Earth⁶ and stellar mass/angular-momentum evolution⁷.

Solar flares, filament eruptions, and CMEs are thought to be caused by the common magne-

tohydrodynamic process, though all of them are not necessarily observed in the same event. Magnetic reconnection is a key energy release mechanism for flares, which are thought to be sometimes be triggered by the instability of cool filaments in active regions¹. Recently, it has been discussed that much larger “superflares” that release the energy of more than 10^{33} erg (10 times the largest solar flares $\sim 10^{32}$ erg) can occur – or have occurred relatively recently – even on the Sun^{3-5,8}. Superflares may produce much larger CMEs than the largest solar flares, which can significantly affect the environment, habitability, and development of life around young and intermediate age stars⁶. However, superflares on solar-type stars have been mainly detected by optical photometry (e.g., Kepler space telescope)³. Therefore, no observational indication of filament eruptions/CMEs has been reported for solar-type stars. Optical spectroscopic observations are a promising way to detect stellar filament eruptions, which can be indirect evidence of CMEs. However, for solar-type stars, optical spectra of superflares have never been obtained.

EK Draconis (EK Dra) is known to be an active young solar-type star (a G-type, zero-age main-sequence star with an effective temperature of 5560–5700 K and age of 50–125 million years⁹) that exhibits frequent UV stellar flares^{10,11} and gigantic starspots at low-high latitudes⁹. We conducted optical spectroscopic monitoring of EK Dra for 19 nights between 21 January 2020 and 15 April 2020, simultaneously with optical photometry from the Transiting Exoplanet Survey Satellite (TESS)¹². Time-resolved neutral-hydrogen H α -line spectra at 6562.8 Å (radiation from cool plasma of a few times 10,000 K) were spectroscopically observed at the 3.8-m Seimei Telescope¹³ and the 2-m Nayuta Telescope. In this campaign, we succeeded in obtaining optical spectra of large superflares on a solar-type star. The superflare that occurred on 5 April 2020 was

simultaneously observed using TESS photometry in white light ($\sim 6,000\text{--}10,000\text{ \AA}$) and ground-based spectroscopy in $H\alpha$ line (Fig. 1a-b and Extended Data Fig. 1). The $H\alpha$ brightening was associated with the TESS white-light flare, which lasted 16 ± 2 min. The radiated bolometric energy of the TESS white-light flare is estimated to be $2.0 \pm 0.1 \times 10^{33}$ erg (20 times the most energetic solar flares), and the radiated $H\alpha$ -line energy was $1.7 \pm 0.1 \times 10^{31}$ erg; thus, the flare is classified as a superflare.

After the impulsive phase, the TESS white-light intensity returned to its pre-flare level. However, the equivalent width (hereafter E.W.) of $H\alpha$ (the wavelength-integrated $H\alpha$ emission normalized by the continuum level) became lower than the pre-flare level (i.e., it displayed enhanced absorption), returning to the pre-flare level in approximately 2 hours (Fig. 1b). The blue-shift $H\alpha$ absorption component with a maximum central velocity of about -510 km s^{-1} and a half-width of $\pm 220\text{ km s}^{-1}$ appeared soon after the superflare. The velocity gradually slowed down with time, and a red-shifted absorption component appeared at a few times 10 km s^{-1} (Fig. 1c-e, Extended Data Fig. 2a, 3a). Both ground-based spectroscopic observations simultaneously recorded the same spectral change, demonstrating that low-temperature and high-density neutral plasma above the stellar disk moves at high speed toward the observer before some parts finally start to fall back to the surface. In addition, the deceleration is not monotonic: it was $0.34 \pm 0.04\text{ km s}^{-2}$ in the initial phase, dropping to $0.016 \pm 0.008\text{ km s}^{-2}$ in the later phase (Fig. 1c-d and Extended Data Fig. 3b). This is interpreted in terms of changes in the height of the ejected mass. The observed deceleration is in good agreement with that due to the surface gravity of approximately $0.30 \pm 0.05\text{ km s}^{-2}$ (ref.⁹), although the initial value is slightly larger.

How much do the stellar spectral changes obtained here actually resemble those of solar filament eruptions? Blue-shifted $H\alpha$ absorption profiles are often observed from solar filament eruptions^{1,14}. As in Fig. 2, we generated spatially-integrated $H\alpha$ spectra of a solar flare/filament eruption that occurred on the solar disk using the SMART data¹⁵ (Extended Data Fig. 4, Supplementary Movie 1). We converted to the full-disk pre-flare subtracted spectra by multiplying by the partial-region/full-disk ratio (i.e., virtual Sun-as-a-star spectra). We found that the blue-shifted absorption component at approximately 100 km s^{-1} was predominant soon after the solar flare, and the spatially integrated $H\alpha$ E.W. showed enhanced absorption (Fig. 2a). These blue-shifted profiles are unequivocally due to the filament eruption. Later, the blue-shifted component decelerated and gradually turned into slow, red-shifted absorption (Fig. 2b-c). The $H\alpha$ E.W. returned to the pre-flare level in approximately 40 min (Fig. 2a). Although the energy scales and velocities are different, the solar data greatly resembles the spectral changes in the superflare on EK Dra (see Supplementary Information for another event). This similarity suggests that the stellar phenomenon is the same as the simply magnified picture of the solar filament eruption.

A filament eruption is the only explanation for the blue-shifted absorption component on EK Dra by solar analogy¹. The hypothesis that the blue-shifted absorption on EK Dra might come from up-/down-flow in flare kernels must be rejected because they never show $H\alpha$ absorption^{16,17}. Also, down-flow in cooled magnetic loops (known as post-flare loops)¹⁴ show red-shifted absorption, so they cannot explain the blue-shifted absorption. (However, the red-shifted absorption in EK Dra in the later phase might be caused by post-flare loops¹⁴.) Rotational visibilities of prominences or spots also are not adequate to explain it since the rotation speed of EK Dra is only $16.4 \pm 0.1 \text{ km}$

s^{-1} (ref.⁹). Thus, we concluded that we detected a stellar filament eruption on the solar-type star.

Some observational signatures for stellar filament eruptions or CMEs have been reported previously for cooler K-M dwarfs^{18–21,23} and evolved giant stars²² (see Methods and ref.^{6,24} for review). The observation of a giant star shows a blue-shifted X-ray emission line of 90 km s^{-1} in the post-flare phase and hotter-CME is proposed as a possible explanation²². Recently, X-ray/EUV dimmings are reported as an indirect evidence of stellar CMEs on K-M dwarfs²³. In M-dwarf flares, many blue-shifted Balmer/UV line emission components have been reported^{18–21,24}, which are interpreted as filament eruptions. Some M-dwarf flares share properties similar to the eruption on EK Dra: the blue-shift emissions have high velocities of hundreds of km s^{-1} , and some exhibit velocity changes and appear after the impulsive phase^{20,21}. For M-dwarf events, the number of studies reporting highly-time-resolved velocity variations of blue-shift components is still insignificant (~ 5 -min cadence), and simultaneous white-light flare has never been detected. Our detection of a stellar filament eruption is reliable because we provided solar counterparts, highly time-resolved spectra (~ 50 -sec cadence), and simultaneous TESS white-light flare.

What properties does the filament eruption on EK Dra have? The maximum observed velocity of the blue-shifted component was $\sim -510 \text{ km s}^{-1}$ with a width of 220 km s^{-1} . This is larger than the typical velocities of solar filament eruptions ($10\text{--}400 \text{ km s}^{-1}$) associated with CMEs², although it is a little smaller than the escape velocity at the surface on EK Dra ($\sim 670 \text{ km s}^{-1}$). The cool plasma reached at least ~ 1.0 stellar radii from the stellar surface (or the initial height) as derived by integrating the velocity over time (or ~ 3.2 stellar radii from the stellar surface based

on the deceleration rates). In this case, the projection angle can be allowed at most 45° when we assume the event occurs on the disk center. On this projection angle, the velocity can be up to $\sim -720 \text{ km s}^{-1}$, so there is a possibility that the velocities of some components of the EK Dra eruption could exceed the escape velocity. However, it should be noted that there are weak red-shifted components with a velocity of a few 10 km s^{-1} in the late phase, indicating some materials fell back to the star. This is often observed in the case of solar filament eruptions with CMEs²⁵.

The filament area is estimated to be $1.6 \times 10^{21} \text{ cm}^2$ (5.6 % of the stellar disk), and the erupted mass is calculated to be $1.1_{-0.9}^{+4.2} \times 10^{18} \text{ g}$ based on the absorption components. The mass is more than 10 times larger than those of the largest solar CMEs^{28,29} (it should be noted that the mass can be somewhat under-/over-estimated, see Methods). This mass estimate is in reasonable agreement with those predicted from empirical^{28,29}, and theoretical³⁰ solar scaling relations between CME mass and flare energy within the error bars ($\sim 9.4_{-2.4}^{+3.2} \times 10^{16}$ and $3.1_{-1.1}^{+1.6} \times 10^{17} \text{ g}$ for ref.²⁹ and ref.²⁸, respectively) (Fig. 3a). This suggests that the stellar filament eruption can share the common underlying mechanism with smaller-scale filament eruptions/CMEs (i.e., magnetic energy release^{1,30}) although the absolute values of most physical quantities are very different.

Moreover, the kinetic energy is calculated to be $3.5_{-3.0}^{+14.0} \times 10^{32} \text{ erg}$, which is 16 % of radiation energy in white light. The magnetic energy stored around the starspots on EK Dra can be at least $8.0 \times 10^{35} \text{ erg}$, which is enough to produce superflares and filament eruptions with energy of $\sim 10^{33} \text{ erg}$. In addition, this value is slightly smaller than those extrapolated from the solar CME scaling law ($4.8_{-0.9}^{+1.1} \times 10^{33} \text{ erg}$; ref.²⁹) (Fig. 3b), which is similar to the filament eruption/CME candidates

on other stars²⁴. In previous studies, it has been argued that kinetic energy can be reduced by overlaying magnetic fields^{24,27}. The deceleration of our events was a few times 10 % larger than the stellar gravity (Extended Data Fig. 3b). The strong magnetic fields on EK Dra were reported before⁹ and may support the above explanations. However, its small kinetic energy can also be understood through a solar analogy: The velocities of (lower-lying) filament eruptions are usually 4-8 times slower than those of the corresponding (higher-lying) CMEs², and therefore the kinetic energies of filament eruptions are typically smaller (green symbols in Fig. 3b).

Did a CME occur in this event? Obviously, the line-of-sight velocity $\sim 510 \text{ km s}^{-1}$ was slower than the escape velocity and some masses fell back, which may indicate a so-called “failed” filament eruption²⁷. However, this does not necessarily mean that a CME did not occur, again by solar analogy. In fact, the erupted filaments often fall back to the Sun while CMEs happen. For example, a well-studied solar event on 2011 June 7 involved a 200-600 km/s filament eruption where lots of filamentary material fell back to the Sun, but some mass clearly escapes as a CME with velocities of $\sim 1000 \text{ km s}^{-1}$ (see ref.²⁵ and Supplementary Information). The event on EK Dra may correspond to this solar event. In addition, ref.²⁶ showed that whether a solar filament eruption leads to a CME can be simply distinguished by a parameter of $(V_{r_max}/100 \text{ km s}^{-1})(L/100 \text{ Mm})^{0.96}$, where V_{r_max} is the maximum radial velocity and L is the length scale (Fig. 4). When the parameter is more than ~ 0.8 , the probability that a filament eruption lead to a CME is more than 90%²⁶. The value of the parameter of eruption on EK Dra is ~ 18 , meaning that our detection of the fast and sizeable stellar filament eruption is indirect evidence that mass escapes into interplanetary space as a CME.

Finally, we summarize future directions of our findings (see Supplementary Information for details): It is speculated that the filament eruptions/CMEs associated with superflares can severely affect planetary atmospheres⁶. Our findings can therefore provide a proxy for the possible enormous filament eruptions on young solar-type stars and the Sun, which would enable us to evaluate the effects on the ancient, young Solar-System planets and the Earth, respectively. Further, it is also speculated that stellar mass loss due to filament eruptions/CMEs can more significantly affect the evolutionary theory of stellar mass, angular momentum, and luminosity^{7,28}, than stellar winds. At present, frequency and statical properties of CMEs on solar-type star is unknown, but important insights into these points are obtained by increasing the samples in the future.

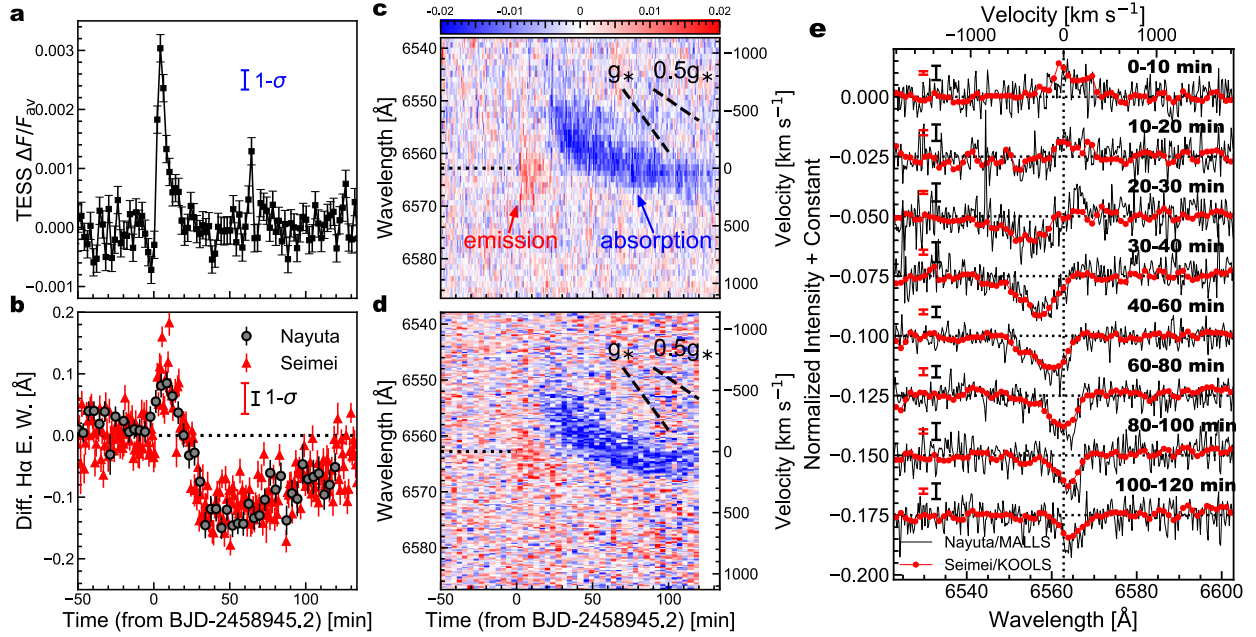


Fig. 1: Light curves (a-b) and spectra (c-e) of a superflare on EK Dra. (a) The light curve observed by TESS in white light ($\sim 6000\text{--}10,000\text{ \AA}$) on BJD (Barycentric Julian Day) 2458945.2 (5 April 2020). The individual points represent the stellar flux normalized by the averaged value with the pre-flare level subtracted. The $1\text{-}\sigma$ value of the pre-flare light curve (-150 min to 0 min) is plotted in blue. (b) Light curves of the $H\alpha$ equivalent width (E.W.) observed by the medium-dispersion spectroscopy MALLS at the Nayuta telescope (grey circles) and the low-dispersion spectrograph KOOLS-IFU installed at the Seimei telescope (red triangles) during the same observing period as in panel (c). The $H\alpha$ emissions were integrated within $\pm 10\text{ \AA}$ from the $H\alpha$ line center (6562.8 \AA) after dividing by the continuum level, and the pre-flare level is subtracted. The positive and negative values represent emission and absorption, respectively, compared to the pre-flare level. The $1\text{-}\sigma$ value of the pre-flare light curve (-150 min to 0 min) is plotted with red and black color for Seimei and Nayuta data, respectively. (c-d) Two-dimensional $H\alpha$ spectra obtained by the Seimei Telescope (c) and the Nayuta Telescope (d). The red and blue colors correspond to emission and absorption, respectively. The dashed lines indicate the stellar surface gravity (g_*) and half of the surface gravity ($0.5 g_*$). The panels (c-d) share the upper color bar. (e) Temporal evolution of the pre-flare-subtracted $H\alpha$ spectra observed by the Seimei telescope (red) and the Nayuta telescope (black), with the spectra shifted by constant values for clarity. The spectra are binned in time, and the integration periods correspond to the horizontal axes of panels (a-d). The intensities are normalized by the stellar continuum level. The vertical dotted line indicates the $H\alpha$ line center, and the horizontal dotted lines indicate the zero levels for each spectrum. The $1\text{-}\sigma$ error bar around the line core is also plotted based on the residual scattering in the line wing.

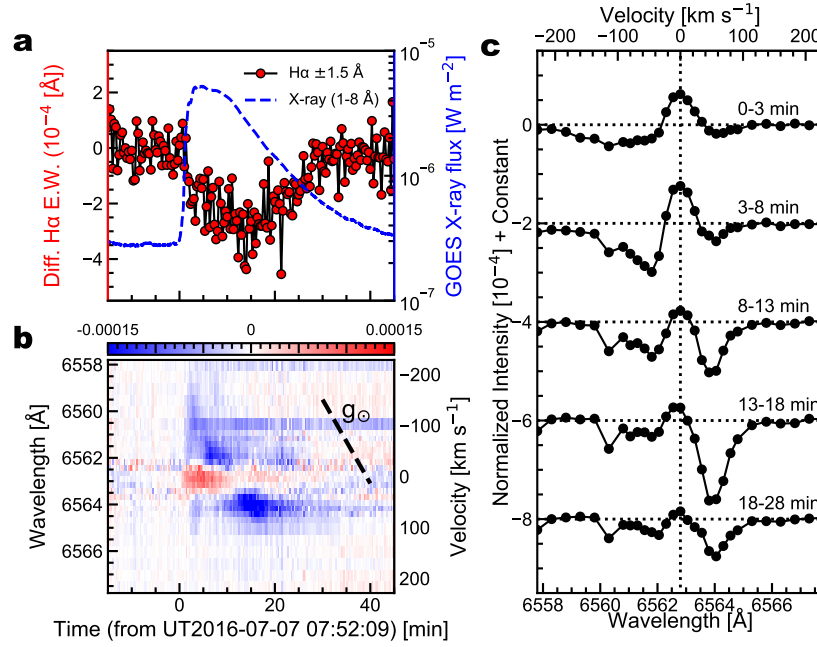


Fig. 2: The space-integrated light curves (a) and spectra (b-c) of a C5.1-class solar flare and filament eruption on 7 July, 2016, observed with the SDDI installed at the SMART telescope. (a) GOES soft X-ray (1-8 Å) and H α E.W. light curves of the solar flare are plotted as a blue dashed line and red circles, respectively. The H α emissions were integrated within ± 1.5 Å from the H α line center (6562.8 Å) and were divided by the full-disk continuum level, and the pre-flare level is subtracted. Time 0 is the time when the flare begins. (b) Two-dimensional pre-flare-subtracted H α spectra. The red and blue colors correspond to emission and absorption compared to the pre-flare levels, respectively. The dashed line indicates surface gravity at the solar surface. (c) Temporal evolution of the pre-flare-subtracted H α spectrum shifted vertically by constant values for clarity. The H α spectra were produced by integrating the data over a large enough region to cover the flaring area (see Extended Data Fig. 4). The intensities are normalized by the total solar continuum level. The vertical dotted line indicates the H α line center, and the horizontal dotted lines indicate the zero levels for each spectrum.

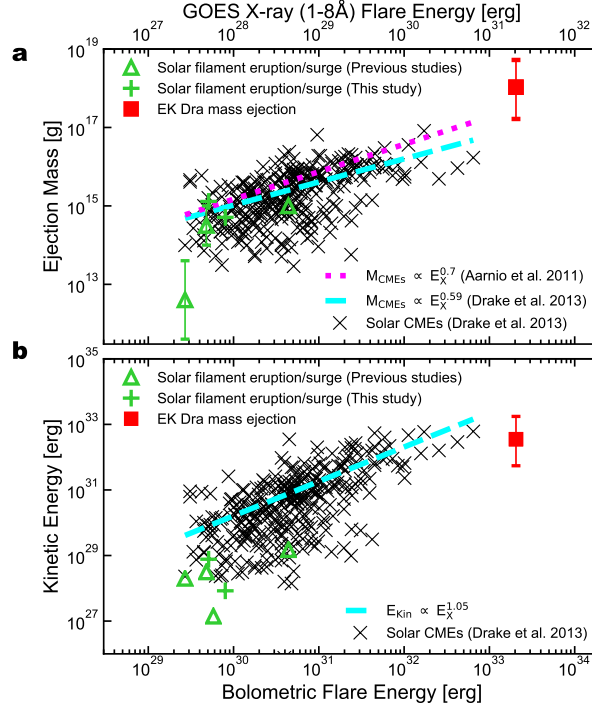


Fig. 3: Mass and kinetic energy as a function of flare energy for solar and stellar flares and filament eruptions/CMEs. (a) Comparison between bolometric flare energy and ejected mass. The red square represents the superflare on EK Dra, the black crosses denote for solar CME data, the green triangles are data for solar prominence/filament eruptions and surges taken from previous studies, and the green plus sign signifies the solar filament eruption/surges displayed in Fig. 2 and Supplementary Fig. 9 (Supplementary Information “Velocity, mass, and kinetic energy: solar data”), respectively (see Table 1). Note that solar “surges” are jet-like filament eruption phenomena (see Supplementary Information section “Another case of solar flares on 2 April 2017” for the explanation of the surge). The cyan dashed, and magenta dotted lines are trend fits for solar CMEs expressed as $M_{\text{CMEs}} \propto E^{0.59}$ and $M_{\text{CMEs}} \propto E^{0.7}$, respectively (see Supplementary Information section “Solar flare energy-CME mass relation” and and ref.^{28,29}).

(b) Comparison between flare bolometric energy and kinetic energy of the erupted mass. The symbols are the same as in panel (a). The cyan dashed line is a fit for solar CMEs expressed as $E_{\text{Kin}} \propto E_X^{1.05}$. The kinetic energy of eruption on EK Dra is calculated to be $3.5_{-3.0}^{+14.0} \times 10^{32}$ erg, which is outside the error range of the predicted value of $4.8_{-0.9}^{+1.1} \times 10^{33}$ erg; ref.²⁹.

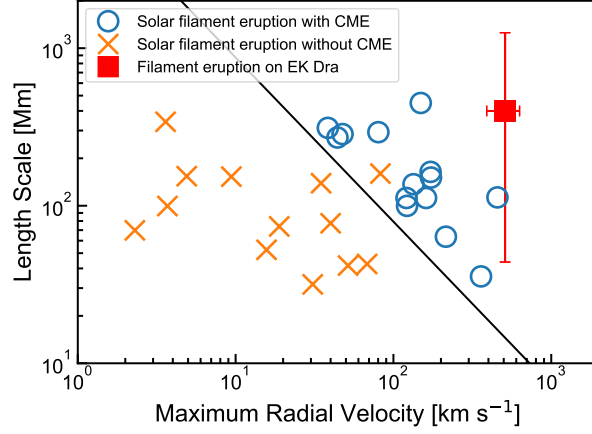


Fig. 4: Statistical properties of solar filament eruptions taken from ref.²⁶ and comparison with the stellar filament eruption on EK Dra. The figure shows the comparison between maximum radial velocities (V_{r_max}) and length scales (L) of filament eruptions. The blue circles and orange crosses indicate the solar filament eruptions with and without CMEs, respectively. The red point corresponds to the stellar filament eruption on EK Dra obtained here (see Methods section “Velocity, mass, and kinetic energy: stellar data” for the calculation of the length scale). Note that the stellar data are the observed line-of-sight velocity. Since the deceleration of the stellar filament eruption corresponds well with the surface gravity and the absorption component of filament is visible on the disk all time, we can expect that the filament is flying in our direction perpendicularly to some extent, so there would not be such a big difference between radial velocity and line-of-sight velocity. We expect that the radial velocity can be larger than the line-of-sight velocity if we assume the projection effect, while it will be about $\sqrt{2}$ times smaller at most if it erupts at a 45-degree tilt in the radial direction, which does not change our discussion. The solid line indicates the threshold that can roughly distinguish filament eruption with and without CMEs derived by ref.²⁶. The threshold can be expressed as $(V_{r_max}/100 \text{ km s}^{-1}) (L/100 \text{ Mm})^{0.96} = 0.8$, which is determined by using the algorithm of Linear Support Vector Classification (see ref.²⁶ for the detailed method).

Date	GOES	flare energy	mass	kinetic energy	reference	event
yyyy/mm/dd		[10^{29} erg]	[g]	[erg]		
1980/10/30	C4.8	4.5	10^{14-15}	3.14×10^{28}	Ref. ⁴³	surge
2001/8/30	C5.8	5.5	-	1.4×10^{27}	Ref. ⁴⁴	surge
1993/5/14	M4.4	44	10^{15}	1.5×10^{29}	Ref. ⁴⁵	filament eruption
2012/2/11	C2.7	2.7	$4 \times 10^{11-13}$	2×10^{28}	Ref. ⁴⁶	filament eruption
2016/7/7	C5.1	5.1	1.3×10^{15}	7.7×10^{28}	Event-1	filament eruption
2017/4/2	C8.0	8.0	5.1×10^{14}	8.5×10^{27}	Event-2 [†]	surge

[†] The analysis of the solar surge (Event-2) is described in Supplementary Information section

“Another case of solar flares on 2 April 2017”.

Table 1: Properties of solar filament eruptions/surges reported in previous studies and this study. The data are plotted in Figure 3. The calculation of flare energy, mass, and kinetic energy is introduced in Supplementary Information section “Velocity, mass, and kinetic energy: solar data”.

Methods

TESS light-curve analysis TESS observed EK Dra (TIC 159613900) in its sector 14-16 (18 July 2019-6 October 2020) and 21-23 (21 January 2020-15 April 2020). The TESS light curve from the 2-min time-cadence photometry was processed by the Science Processing Operations Center pipeline, a descendant of the Kepler mission pipeline based at the NASA Ames Research Center^{12,31}. Extended Data Fig. 1 shows the light curve of the EK Dra from BJD (Barycentric Julian Day) 2458945 (= JD 2458944.997 = 5 April 2020 11:56UT; Sector 23), and the stellar superflare detected by TESS, Seimei telescope, and Nayuta telescope in Fig. 1 is indicated with the red arrow in this figure. The quasi-periodic brightness variation is thought to be caused by the rotation of EK Dra with the asymmetrically-spotted hemisphere^{3,5}. The rotation period is reported as about 2.8 days⁹. Although the superflare occurred near the local brightness maximum, some of the starspots are expected to be visible from the observer³⁴⁻³⁷. In Extended Data Fig. 1, other flares are also indicated with black arrows with more than two consecutive observational points whose flaring amplitude is more than 3 times TESS photometric errors^{3,32}. The white-light flare energy was calculated by assuming the 10,000 K blackbody spectra^{32,33} (see, Supplementary Information section “Flare energy”). The pixel-level data analysis is shown in Supplementary Information section “TESS pixel-level data analysis”. The estimated flare occurrence frequency of superflares ($> 10^{33}$ erg) in the TESS band was about once per 2 days, which means that about-twelve-nights monitoring observations are necessary on average to detect one superflare from the ground-based telescope under the clear-sky ratio of 50 %. This implies that our datasets are highly unique.

Spectroscopic data analysis Here, we present the utilization of low-resolution spectroscopic data from KOOLS-IFU³⁸ (Kyoto Okayama Optical Low-dispersion Spectrograph with optical-fiber Integral Field Unit) of the 3.8-m Seimei Telescope¹³ at Okayama Observatory of Kyoto University and MALLS^{19,39} (Medium And Low-dispersion Long-slit Spectrograph) of the 2-m Nayuta Telescope at Nishi-Harima Astronomical Observatory of University of Hyogo. KOOLS-IFU is an optical spectrograph with a spectral resolution of $R (\lambda/\Delta\lambda) \sim 2,000$ covering a wavelength range from 5800 to 8000 Å; it is equipped with Ne gas emission lines for wavelength calibration and instrument characterization. The exposure time was set to be 30 sec for this night. The sky spectrum was subtracted by using the sky fibers for each spectrum. The data reduction follows the prescription in ref.⁴⁰. During this observation, the signal-to-noise ratio (S/N) for one frame is typically 172 ± 6 . The observations by Seimei Telescope ended just after 133.7 min in Fig. 1b-d.

MALLS is optical spectroscopy with a spectral resolution of $R \sim 10,000$ at the $H\alpha$ line covering a wavelength range from 6350 to 6800 Å; it is also equipped with Fe, Ne, and Ar gas emission lines for wavelength calibration and instrument characterization. The sky spectrum was subtracted using a nearby region along the slit direction for each observation. The exposure time was set to be 3 min for this night. The MALLS data reduction follows the prescription in ref.¹⁹. The signal-to-noise ratio (S/N) for one frame is typically 86 ± 8 during this observation. For the MALLS data, the wavelength corrections are also performed for each spectrum by using the Earth's atmospheric absorption lines.

We corrected the wavelength for the proper motion velocity of -20.7 km s^{-1} of EK Dra based on Gaia Data Release 2 (ref.⁴¹). Continuum levels are defined by fitting with the linear line

between the wavelength range of H α line wing (6517.8-6537.8 and 6587.8-6607.8 Å). We take the continuum level as the wavelength range of 6517.8-6537.8 and 6587.8-6607.8 Å to measure the E.W. ($= \int (1 - F_\lambda/F_0)d\lambda$, where F_0 is the continuum intensity on either side of the absorption feature, while F_λ represents the intensity across the entire wavelength range of interest). The original spectra are shown in Supplementary Information section “Stability of pre-flare spectra”. Extended Data Fig. 2 shows the pre-flare-subtracted H α spectra during and after the superflare on EK Dra with higher time cadence than Fig. 1e. The narrow-band H α E.W. (H α - 10 Å \sim H α + 10 Å) is used for the measurements of the radiated energy and duration of H α flare because of the high S/N, and the broad-band H α E.W. (H α - 20 Å \sim H α + 10 Å) is used for the measurements of the amount of absorption (i.e., mass and kinetic energy).

Solar data analysis In the main text, we showed the data of a C5.1-class solar flare (i.e., the peak GOES soft X-ray flux F_{GOES} is $5.1 \times 10^{-6} \text{ W m}^{-2}$, hereafter “Event-1”) and associated filament eruption around 07:56 UT, 7 July 2016 observed by the SDDI (Solar Dynamics Doppler Imager)¹⁵ installed on the SMART (the Solar Magnetic Activity Research Telescope) at Hida Observatory (further explanations continue to the Supplementary Information “Solar data analysis (continued from Methods)”). The SDDI conducted a monitoring observation of the Sun on 7 July 2016. It takes full-disk solar images at 41 wavelength points at every 0.5 Å from the H α line center -9.0 Å (-411 km s^{-1}) to the H α line center $+8.0$ Å (411 km s^{-1}), while it takes the images at every 0.25 Å from the H α line center -2.0 Å (-91 km s^{-1}) to the H α line center $+2.0$ Å (91 km s^{-1}). Each set of images is obtained with a time cadence of 20 seconds and a pixel size of about 1.2 arcsec. The SDDI started the daily monitoring observations in 2016, and the C5.1-class solar flare

is one of the largest solar flares with a filament eruption among the events observed by SDDI with good weather conditions in these 5 years. The solar filament eruption was also reported in ref.^{15,42}. Another jet-like filament eruption (known as solar “surge”¹) associated with a C8.0-class solar flare is also shown in the Supplementary Information section “Another case of solar flares on 2 April 2017” (hereafter we call this surge “Event-2”).

This paper used 70-min time series of the SDDI images taken from 07:30 UT on 7 July 2016 (see, Supplementary Movie 1). As in Extended Data Fig. 4, the C5.1-class flare occurred around an active region, named “NOAA 12561”, on the solar disk and was accompanied by a typical filament eruption^{15,42}. The spectra from the event are integrated over a spatial region that is large enough to cover the visible phenomena (the magenta region in Extended Data Fig. 4a-b). The spectra are reconstructed by using the template solar H α spectrum convolved with SDDI instrumental profile.

Here, we define $L(\lambda, t, A)$ as a luminosity at a wavelength of λ and time of t which is integrated for the region A (i.e., $L(\lambda, t, A) = \int_A I(t) dA$, $I(t)$ is intensity). We now define A_{local} as the integration region (magenta region in Extended Data Fig. 4a-b), and $A_{\text{full-disk}}$ as the solar full disk. We first obtained the local (partial-image) pre-flare subtracted spectra ΔS_{local} which are normalized by local (partial-image) total continuum level ($L(6570.8\text{\AA}, t, A_{\text{local}})$):

$$\Delta S_{\text{local}} = \frac{L(\lambda, t, A_{\text{local}}) - L(\lambda, t_0, A_{\text{local}})}{L(6570.8\text{\AA}, t, A_{\text{local}})}, \quad (1)$$

where t_0 is a given time of the pre-flare period. Then, the (virtual) full-disk pre-flare-subtracted spectra $\Delta S_{\text{full-disk}}$ are obtained by multiplying the ratio of the partial-image continuum to full-disk

continuum (total continuum ratio:

$$\Delta S_{\text{full-disk}} = \Delta S_{\text{local}} \times \frac{L(6571.8\text{\AA}, t_0, A_{\text{local}})}{L(6570.8\text{\AA}, t_0, A_{\text{full-disk}})}, \quad (2)$$

then we obtained a virtual pre-flare-subtracted spectrum of this phenomena as if we observed the Sun as a star.

The E.W. of the $H\alpha$ is also calculated by using the full-disk-normalized and pre-flare-subtracted spectra ($\Delta S_{\text{full-disk}}$), and we obtained the virtual Sun-as-a-star $\Delta H\alpha$ E.W. (i.e., differential $H\alpha$ flux normalized by the full-disk continuum level).

Velocity, mass, and kinetic energy: stellar data For the stellar filament eruption, the velocity is derived by fitting the absorption spectra obtained by Seimei telescope with the normal distribution $N(\lambda, \mu, \sigma^2)$ where μ is the mean wavelength and σ^2 is the variance. In Extended Data Fig. 3a, we plotted the temporal evolution of the velocity ($(\mu - \lambda)/\lambda \times c$, where λ is 6562.8 Å, c is light speed) for the fitted absorption feature with the width of σ . We only plotted the data whose absorption features are clear enough to fit the shape with the threshold of the fitted absorption amplitude > 0.01 and fitted velocity dispersion of $< 500 \text{ km s}^{-1}$ and $> 100 \text{ km s}^{-1}$. The threshold was determined by trial and error, and we find that many missed detections of absorption features occur when we select threshold values other than this one. The amplitude value of 0.01 corresponds to the detection limit when considering the typical $S/N \sim 170$ of the Seimei Telescope/KOOLS-IFU, and the lower limit of 100 km s^{-1} is determined to avoid detecting the sharp noisy signals. About 27% of data points were discarded due to this threshold from the initial points (22 min) to final points (110 min), especially for the latter decaying phase. Here, the maximum observed velocity

and its errors are calculated as $510 \pm 120 \text{ km s}^{-1}$ with its width of $220 \pm 90 \text{ km s}^{-1}$ from the mean values of the μ and σ of the first five points ($t = 22\text{-}26 \text{ min}$ in Fig. 1), respectively. The mean values of the velocity when the absorption becomes strong ($t = 25\text{-}50 \text{ min}$ in Fig. 1) is estimated as 258 km s^{-1} .

The plasma mass is simply calculated from the total H α E.W.. We used the simple Becker's cloud model⁴⁹ with optical depth at the line center of the ejected plasma τ_0 of 5 (which is slightly more optically thick than solar filament eruptions; c.f., ref.⁵⁰), the two-dimensional aspect ratio of 1 (i.e., cubic), local plasma dispersion velocity W of 20 km s^{-1} , and source function S of 0.1 based on the solar observations⁴⁸. The observed half width of 220 km s^{-1} of the stellar blue shifted component is larger by one order of magnitude than the solar value, but here we use the solar value as a template. The dispersion velocity of 220 km s^{-1} is considered to be the upper limit of the local velocity dispersion because the ejected mass would have the complex two-dimensional velocity distribution which can cause larger W in the integrated spectra. First, modeled E.W. of enhanced absorption is calculated by using the Becker's cloud model when the plasma velocity v_{shift} is -258 km s^{-1} as

$$\text{model E.W.} = \int_{\lambda} \frac{I_{\lambda} - I_{0\lambda}}{I_{0,\text{Cont.}}} d\lambda = \int_{\lambda} \frac{S - I_{0\lambda}}{I_{0,\text{Cont.}}} (1 - e^{-\tau_{\lambda}}) d\lambda \quad (3)$$

$$\tau_{\lambda} = \tau_0 \exp \left[-\frac{1}{2} \left(\frac{\lambda/\lambda_0 - (1 + v_{\text{shift}}/c)}{W/c} \right)^2 \right], \quad (4)$$

where $I_{0\lambda}$ is background intensity and $I_{0,\text{Cont.}}$ is continuum intensity. This is the E.W. value for an extreme case when the full disk of the star is completely covered with absorbing, cool ejected plasma. By comparing the modeled E.W. (Eq. 3) with the lowest observed stellar E.W. value

of -0.16 \AA (integrated for $H\alpha - 20 \text{ \AA} \sim H\alpha + 10 \text{ \AA}$; see Supplementary Fig. 4c), the cool-plasma filling factor compared to the stellar disk is calculated to be 5.9 % of stellar disk (i.e., modeled E.W./observed E.W.; $Area = 1.6 \times 10^{21} \text{ cm}^2$). Using the length scale of the ejected plasma $3.9 \times 10^{10} \text{ cm}$ ($= Area^{0.5}$), the hydrogen column density is derived as $4.0 \times 10^{20} \text{ cm}^{-2}$ from the assumed optical depth based on the plasma model⁵¹. In the model of ref.⁵¹, hydrogen/electron density is calculated by assuming an ionization equilibrium for a population of hydrogen atoms due to a balance between recombination and radiative photoionization through Balmer/Lyman continuum. It should be noted that the ionization equilibrium of filaments on active stars may be somewhat different from the solar observations due to their high UV radiations, which may affect the evaluation of the mass of the ejecta. By multiplying the hydrogen column density by the filament area, we then obtained the plasma mass of $1.1 \times 10^{18} \text{ g}$. If the two-dimensional aspect ratio becomes 0.1 similar to jet-like feature (x-width:y-width:z-depth = 1:0.1:0.1), then the estimated mass becomes larger by a factor of 1.78. If optical depth ranges from 0.8 to 10 (ref.⁵⁰), the source function takes values of 0.02 or 0.5, and the dispersion velocity takes 10 or 220 km s^{-1} ⁴⁸, the estimated masses change by a factor of from 0.15 to 4.9. In Fig. 3a, we used the mass of $1.1_{-0.9}^{+4.2} \times 10^{18} \text{ g}$ for optical depth of 5, and uncertainties of the model (0.15-4.9) are used as the error bars since the model-based errors are expected to be much larger than the observational errors. It should be noted that this mass estimate could be either a significant overestimate of the mass of an affiliated CME due to most of the filament falling back to the star, or it could be a significant underestimate due to most of the CME actually being hot coronal material rather than cool filament. The plasma kinetic energy is then calculated as $3.5_{-3.0}^{+14.0} \times 10^{32} \text{ erg}$ by using the velocity of 258 km s^{-1} . The observed

maximum velocity was 510 km s^{-1} in the early phase, so the kinetic energy can be larger by a factor of 4 although the absorption component was weak at that time.

Related works on candidates of stellar filament eruptions/CMEs on other types of stars Here, we discuss potential stellar filament eruptions/CMEs reported in the previous studies (see^{6,24,86} for review). In other stars, such as M-type stars^{18–21,21,53–61}, K-type stars⁵², T-Tauri stars^{62,66}, close binaries^{67,71}, and giant stars²², some observational candidates of stellar filament eruptions/CMEs have been reported, although confirmations of filament eruptions/CMEs in analogy with solar observations are still rare. We also note that some other studies have tried to detect a signature of stellar filament eruptions/CMEs in various ways but have not succeeded in robust detection^{73–80}.

A signature of CME was reported from a blue-shifted emission component of the cool X-ray O VIII line (4 MK) in the late phase of stellar flare on an evolved giant star HR 9024²². Although the time evolution of the blue-shifted velocity is not obtained there, they detected the blue-shifted emission component with a velocity of 90 km s^{-1} (the escape velocity 220 km s^{-1}) and interpreted it as a CME. The blue-shifted plasma components with a few MK are also emitted from the upward flow in the confined flare loops (called “chromospheric evaporation”) in the case of solar flares, but they exclude the possibility considering that the other hotter lines do not show the blue-shifted component in the post-flare phase. Although the spectral-type of HD 9024 (evolved giant star) is very different from EK Dra and the velocity (90 km s^{-1}) is smaller than our observation (510 km s^{-1}), both observations share the same trend that mass ejection signatures is dominant in the post-flare phase.

Blue-shifted emission components of chromospheric lines have been reported in association with the Balmer-line flares mostly on active M/K dwarfs^{18–21,52–61} (see ref.^{24,50} for the summary). The time-varying blue-shifted hydrogen emission components have also been reported with high time cadence on M dwarfs (e.g., ref.^{19,21}). A similar case is reported for a UV flare on an M dwarf^{20,70}. These can be possible evidence of stellar prominence eruptions/CMEs. It seems quite possible that the blue-shifted emission lines on M-dwarfs are very analogous to the $H\alpha$ absorption signatures studied in this paper. The fundamental differences between G-dwarf and M-dwarf blue-shift signature is that for hotter G dwarfs, $H\alpha$ in an erupting filament will only be detectable in absorption, whereas for the cooler M dwarfs even the quiescent $H\alpha$ line is in emission, so an erupting filament might be observed in emission as well (cf. ref.⁵⁰). Blue-wing enhancements of M-dwarf flares is characterized by the high velocity of several hundred km s^{-1} (sometimes more than that)^{18,53,53,60}, which cannot be explained by chromospheric-line blue-shift phenomena associated chromospheric evaporation flow observed in solar flares^{16,50,81–84}. The high velocity of M-dwarf flares are similar to that detected on EK Dra in this study ($\sim 510 \text{ km s}^{-1}$). In addition, not all but some of the blue-shift events on M dwarfs appear after the impulsive phase^{20,21}, which shares the same properties with filament eruption events on EK Dra and the Sun in this study. Therefore, at present the blue-shifted emission lines in M-type stars are most likely prominence eruptions.

Other signatures of kinematic characteristics of the ejected plasma are also inferred from continuous X-ray absorption during stellar flares, which can be caused by neutral material above the flaring region, such as filament eruptions^{24,63–69}. However, on the Sun, X-ray absorption by promi-

nences is uncommon^{50,85}, and instrumental calibration effects at low energy have been pointed out⁸⁶.

In some cases of binary stars, eclipses of the white dwarf component have been interpreted as obscuration by stellar mass ejected from the late-type companion star^{71,72}. Other than this, pre-flare dips have been reported in stellar flares, suggesting potential prominence eruptions/CMEs^{87,88}. Radio observations have recently investigated the type-II radio bursts associated with shocks in front of CMEs as possible indirect evidence of CMEs, but no significant signature has been obtained so far^{74–80,86}. Recently, a stellar type-IV burst event from the M-type star Proxima Centauri was reported and may be evidence for a stellar CME⁶¹.

Data availability In addition to the figure data available, all raw spectroscopic data are available either in the associated observatory archive (<https://smoka.nao.ac.jp/index.jsp> for KOOLS-IFU data in Figure 1 (available after Jan 2022); <https://www.hida.kyoto-u.ac.jp/SMART/T1.html> for a part of SDDI data in Figure 2) or upon request from the corresponding author (for MALLS data in Figure 1 and full raw data of SDDI). The TESS light curve is available at the MAST archive (<https://mast.stsci.edu/portal/Mashup/Clients/Mast/Portal.html>). All datasets used to make figures are available online.

Acknowledgements Some of the data presented here were obtained at the Okayama Observatory of Kyoto University, which is operated as a scientific partnership with National Astronomical Observatory of Japan. We are grateful to the staff of Okayama Observatory, M. Kurita, M. Kino, F. Iwamuro, K. Ohta, H. Izumiura, K. Matsubayashi, D. Kuroda, and T. Nagata, for the telescope and instrument development. Some of

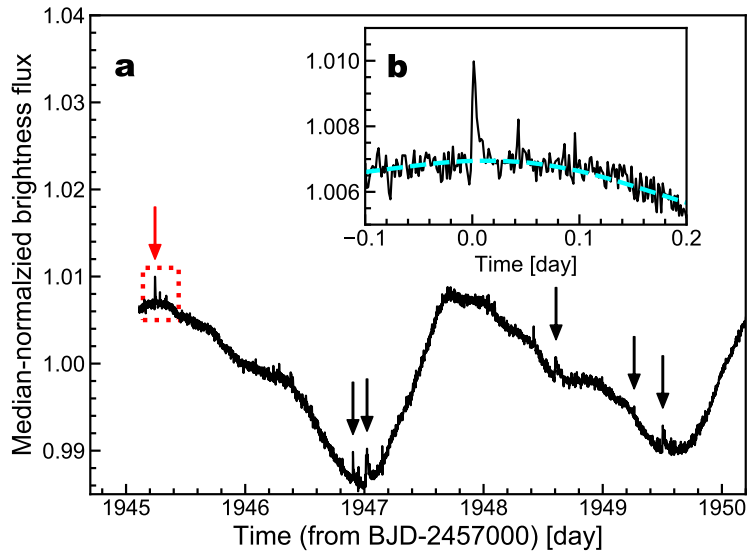
the data presented here were obtained at the Nishi-Harima Astronomical Observatory of the University of Hyogo through the framework of the Optical and Infrared Synergetic Telescopes for Education and Research (OISTER). This work and operations of OISTER were supported by the Optical and Near-infrared Astronomy Inter-University Cooperation Program and the Grants-in-Aid of the Ministry of Education. Some of the solar data presented here were obtained at the Hida Observatory of Kyoto University, which is partly supported by Project for Solar-Terrestrial Environment Prediction (PSTEP). We are grateful to the staff of Hida Observatory for the instrument development and daily observations. We would like to thank A. Asai and K. Otsuji for useful discussions on solar mass ejections. Funding for the TESS mission is provided by NASA's Science Mission directorate. We would like to thank J.J. Drake and S. Yashiro for kindly providing the data of CMEs in their works. We would like to thank A.F. Kowalski for carefully checking the English and contents. We also would like to thank Enago (www.enago.jp) for the English review. K.N. is supported by the JSPS Overseas Challenge Program for Young Researchers. Y.N. was supported by JSPS Overseas Research Fellowship Program. We acknowledge the International Space Science Institute and the supported International Team 464: The Role Of Solar And Stellar Energetic Particles On (Exo)Planetary Habitability (ETERNAL). We thank the anonymous reviewers for their constructive comments, which helped us to improve the manuscript. This research is supported by JSPS KAKENHI grant numbers 18J20048, 21J00316 (K.N.), 17K05400, 20K04032, 20H05643 (H.M.), 21J00106 (Y.N.), 20K14521(K.I.), 21H01131 (K.S., H.M., S.H., K.I. and D.N.) and 15H05814 (K.I.)

Author contributions K.N. led the campaign observations, conducted the data analyses, and wrote the draft of the manuscript; H.M. and S.H. partly contributed to the data analyses; K.N., H.M., S.H., S.O., K.I., and D.N. contributed to the observations at the Seimei telescope; J.T., M.T., T.O., T.S., N.K., and M.T. contributed to the observations at the Nayuta telescope; K.I. and T.T.I. are responsible for instruments and

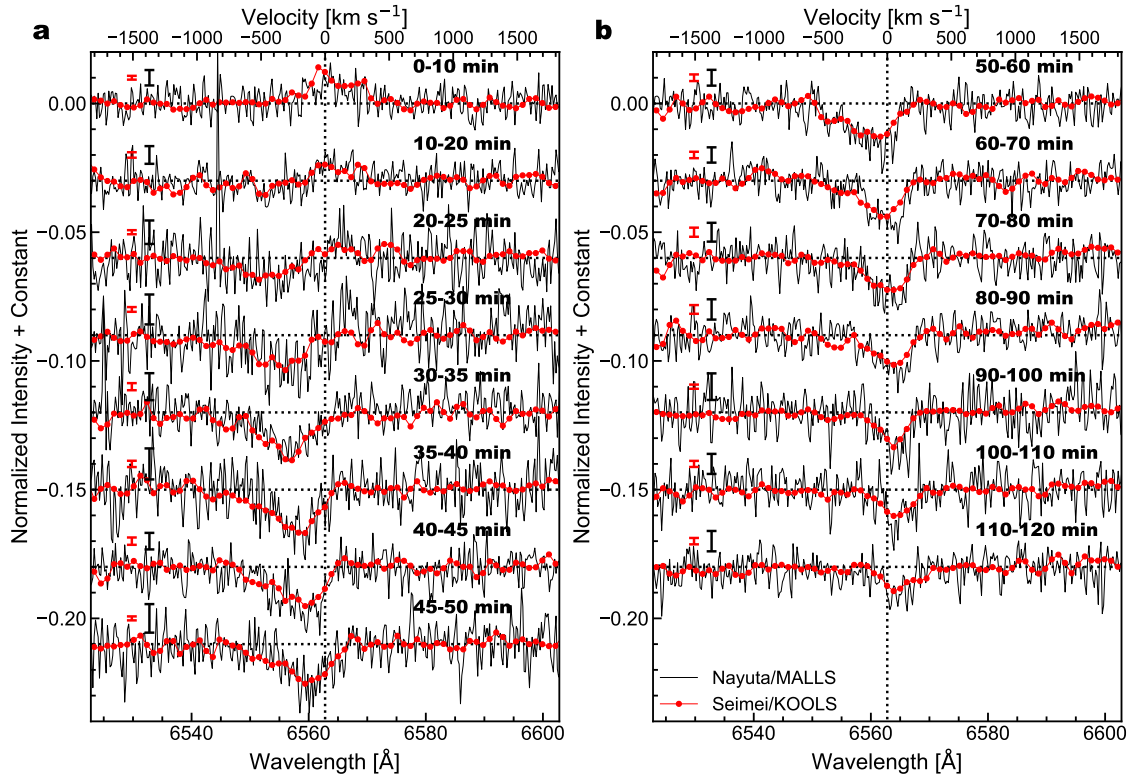
observations at the SMART telescope; H.M., K.L.M., F.O., M.N., R.A., M.O., and M.S. contributed to the ground-based follow-up photometric observations; K.N., H.M., Y.N., D.S., K.I., and K.S. contributed to the data interpretation.

Competing Interests The authors declare that they have no competing financial interests.

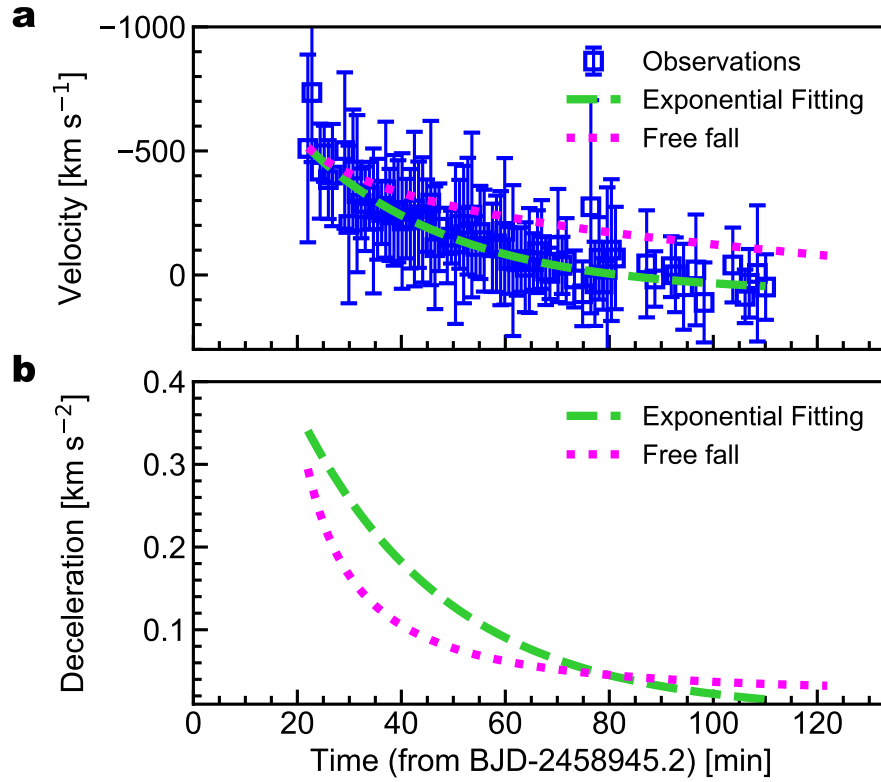
Correspondence Correspondence and requests for materials should be addressed to Kosuke Namekata (email: namekata@kusastro.kyoto-u.ac.jp).



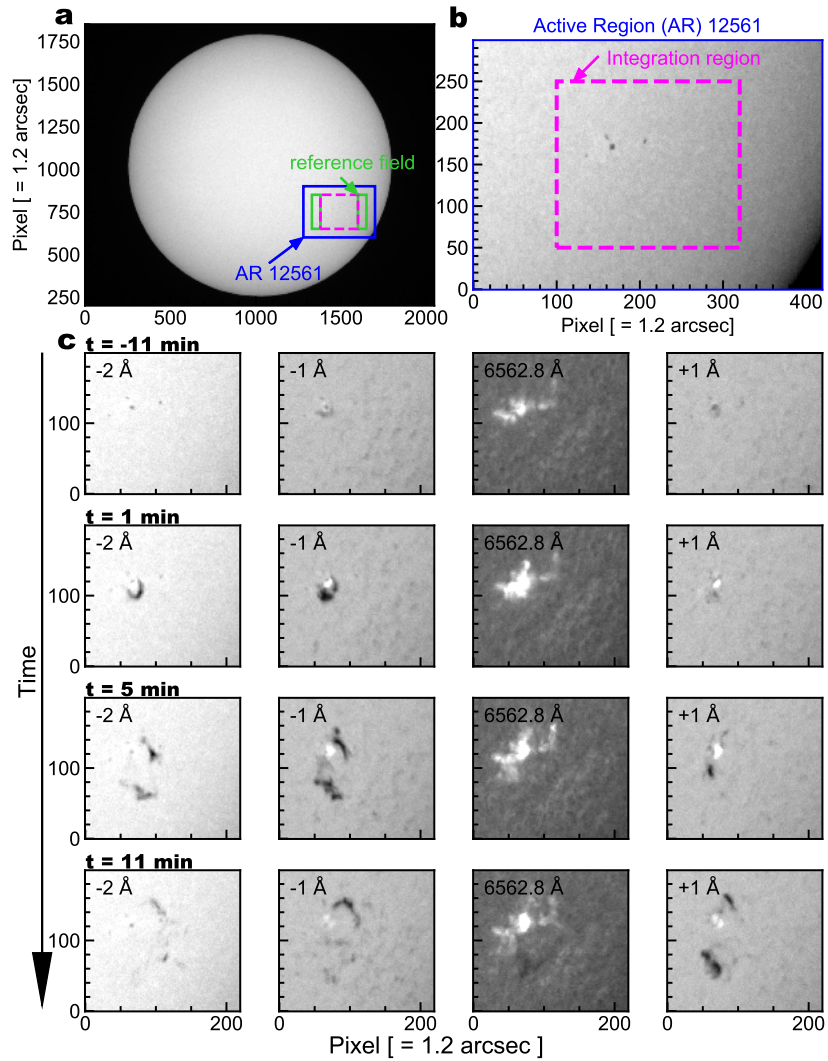
Extended Data Fig. 1: Global TESS light curve for EK Dra. (a) Light curve of a superflare on EK Dra observed by TESS from BJD 2457000. The gap before about BJD 2458945 days corresponds to a gap in the data downlink with Earth during the spacecraft's perigee. The arrows indicate stellar flares that occurred during this observational period, but the other flares in this figure were not observed by ground-based spectroscopic observations. The red arrow is the superflare shown in Fig. 1. (b) Enlarged light curve indicated with the red dotted box in panel (a). The cyan dashed line is the global trend of the light curve caused by the stellar rotation with large starspots.



Extended Data Fig. 2: Pre-flare-subtracted $H\alpha$ spectra during and after the superflare on EK Dra with higher time cadence than panel (e) in Fig. 1. (a, b) The red and black lines are the data observed by the Seimei Telescope and the Nayuta Telescope. The spectra are binned in time, and the integration periods correspond to the horizontal axes of panel (a-d) in Fig. 1. The intensities are normalized by the stellar continuum level. The vertical dotted line indicates the $H\alpha$ line center, and the horizontal dotted lines indicate the zero levels for each spectrum. The $1-\sigma$ values for the line center are indicated with red (Seimei Telescope) and black (Nayuta Telescope) error bars for each time bin. The $1-\sigma$ values are basically calculated by the scattering in line wing (6522.8 - 6532.8 Å and 6592.8 - 6602.8 Å).



Extended Data Fig. 3: Temporal evolution of the velocity and deceleration for the $H\alpha$ -line absorption features. (a) The blue points indicate the velocity of the $H\alpha$ -line absorption features seen after a superflare. The spectra observed by Seimei Telescope were used considering the high S/N and the absorption features are obtained by fitting them with a normal-distribution function. The error bars indicate the standard deviation of the fitted normal distribution. The green dashed line indicates the exponential function which fits the blue symbols, and the magenta dotted line indicates the velocity evolution of the free fall. (b) The temporal evolution of deceleration rates is derived from the velocity changes for observation and free-fall model in panel (a).



Extended Data Fig. 4: A solar flare on 7 July, 2016, observed by SMART telescope/SDDI at Hida observatory. (a) A full disk image of the Sun at the $H\alpha$ line wing (6554.8 Å). The horizontal and vertical axes indicate the x-y axes in the unit of the image pixels whose size is about 1.2 arcsec. The green region is a quiet region used as a reference to make the $H\alpha$ spectra. **(b)** the blue region is the enlarged panel of the active region 12561. The magenta is the region where the solar flare and filament eruption happened. **(c)** The temporal evolution of solar images in the magenta region at a wavelength of 6560.8 (-91 km s^{-1}), 6561.8 (-46 km s^{-1}), 6562.8 (0 km s^{-1}), 6563.8 ($+46 \text{ km s}^{-1}$). The emission and absorption features are indicated with white and black, respectively. The movie is available in Extended Data Movie 1.

1. Shibata, K. & Magara, T. Solar Flares: Magnetohydrodynamic Processes. *Living Rev. Sol. Phys.*, **8**, 6 (2011).
2. Gopalswamy, N. et al., Prominence Eruptions and Coronal Mass Ejection: A Statistical Study Using Microwave Observations. *Astroph. J.*, **586**, 562 (2003).
3. Maehara, H. et al. Superflares on Solar-type stars. *Nat.*, **485**, 478-481 (2012).
4. Shibata, K. et al., Can Superflares Occur on Our Sun?. *Publ. Astron. Soc. Jpn.*, **65**, 49 (2013).
5. Notsu, Y. et al., Do Kepler Superflare Stars Really Include Slowly Rotating Sun-like Stars? — Results Using APO 3.5 m Telescope Spectroscopic Observations and Gaia-DR2 Data. *Astroph. J.*, **876**, 58 (2019).
6. Airapetian, V. S. et al., Impact of space weather on climate and habitability of terrestrial-type exoplanets. *Int. J. Astrobiol.*, **19**, 136 (2020).
7. Osten, R. A. & Wolk, S. J. Connecting Flares and Transient Mass-loss Events in Magnetically Active Stars. *Astroph. J.*, **809**, 79 (2015).
8. Miyake, F. et al. A signature of cosmic-ray increase in AD 774-775 from tree rings in Japan. *Nat.* 486, 240-242. (2012).
9. Waite, I. A. et al., Magnetic fields on young, moderately rotating Sun-like stars - II. EK Draconis (HD 129333). *Mon. Not. R. Astron. Soc.*, **465**, 2076 (2017).
10. Ayres, T. R., The Flare-ona of EK Draconis. *Astroph. J.*, **150**, 7 (2015).

11. Audard, M., Güdel & M., Guinan, E. F., Implications from Extreme-Ultraviolet Observations for Coronal Heating of Active Stars. *Astrophys. J.*, **513**, L53 (1999).
12. Ricker, G. R. et al. Transiting Exoplanet Survey Satellite (TESS). *J. Astron. Telesc. Instrum. Syst.*, **1**, 014003 (2014).
13. Kurita, M. et al., The Seimei telescope project and technical developments. *Publ. Astron. Soc. Jpn.*, **72**, 48 (2020).
14. Schmieder, B. et al., Evidence for Gentle Chromospheric Evaporation during the Gradual Phase of Large Solar Flares. *Astrophys. J.*, **317**, 956 (1987).
15. Ichimoto, K. et al., A New Solar Imaging System for Observing High-Speed Eruptions: Solar Dynamics Doppler Imager (SDDI). *Sol. Phys.*, **292**, 63 (2017).
16. Švestka, Z., Kopecký, M. & Blaha, M., *Bull. Astron. Inst. Czechoslov.* **13**, 37 (1962).
17. Ichimoto, K. & Kurokawa, H. $H\alpha$ Red Asymmetry of Solar Flares. *Sol. Phys.*, **93**, 105 (1984).
18. Houdebine, E. R., Foing, B. H. & Rodono, M. Dynamics of flares on late-type dMe stars. I. Flare mass ejections and stellar evolution. *Astron. Astrophys.*, **238**, 249 (1990).
19. Honda, S. et al., Time-resolved spectroscopic observations of an M-dwarf flare star EV Lacertae during a flare. *Publ. Astron. Soc. Jpn.*, **70**, 62 (2018).
20. Leitzinger, M., et al., Search for indications of stellar mass ejections using FUV spectra. *Astron. Astrophys.*, **536**, A62 (2011)

21. VIDA, K. et al., Investigating magnetic activity in very stable stellar magnetic fields. Long-term photometric and spectroscopic study of the fully convective M4 dwarf V374 Pegasi. *Astron. Astrophys.* **590**, A11 (2016).
22. Argiroffi, C. et al., A stellar flare-coronal mass ejection event revealed by X-ray plasma motions. *Nat. Astron.*, **3**, 742 (2019).
23. Veronig, A. M. et al., Indications of stellar coronal mass ejections through coronal dimmings. *Nat. Astron.*, online (2021).
24. Moschou, S.-P. et al., The Stellar CME-Flare Relation: What Do Historic Observations Reveal?. *Astrophys. J.* **877**, 105 (2019).
25. Wood, B. E., Howard, R. A., & Linton, M. G., Imaging Prominence Eruptions out to 1 AU. *Astrophys. J.* **816**, 67, (2016)
26. Seki, D. et al., Relationship between three-dimensional velocity of filament eruptions and CME association, *Earth, Planets, and Space*, **73**, 58 (2021)
27. Alvarado-Gómez, J. D. et al., Suppression of Coronal Mass Ejections in Active Stars by an Overlying Large-scale Magnetic Field: A Numerical Study. *Astrophys. J.* **862**, 93 (2018).
28. Aarnio, A. N., Matt, S. P., Stassun & K. G. Mass Loss in Pre-main-sequence Stars via Coronal Mass Ejections and Implications for Angular Momentum Loss. *Astrophys. J.* **760**, 9 (2012).
29. Drake, J. J. et al. Implications of Mass and Energy Loss due to Coronal Mass Ejections on Magnetically Active Stars. *Astrophys. J.* **764**, 170 (2013).

30. Takahashi, T., Mizuno, Y. & Shibata, K. Scaling Relations in Coronal Mass Ejections and Energetic Proton Events Associated with Solar Superflares, *Astrophys. J.*, **833**, L8 (2016).
31. Fausnaugh, M. M. et al. TESS Data Release Notes: Sector 23, DR32, (2020)
32. Shibayama, T. et al. Superflares on Solar-type Stars Observed with Kepler. I. Statistical Properties of Superflares. *Astrophys. J. Supplement Series*, **209**, 5, (2013)
33. Namekata, K. et al. Statistical Studies of Solar White-light Flares and Comparisons with Superflares on Solar-type Stars. *Astrophys. J.*, **851**, 91, (2017)
34. Roettenbacher, R. M., Vida, K., The Connection between Starspots and Flares on Main-sequence Kepler Stars. *Astrophys. J.* **868**, 3, (2018)
35. Doyle, L., et al., Investigating the rotational phase of stellar flares on M dwarfs using K2 short cadence data. *Mon. Not. R. Astron. Soc.* **480**, 2153-2164, (2018)
36. Doyle, L., Ramsay, G., & Doyle, J. G., Superflares and variability in solar-type stars with TESS in the Southern hemisphere. *Mon. Not. R. Astron. Soc.* **494**, 3596-3610, (2020)
37. Namekata, K., et al., Temporal Evolution of Spatially Resolved Individual Star Spots on a Planet-hosting Solar-type Star: Kepler-17. *Astrophys. J.* **891**, 103 (2020)
38. Matsubayashi, K. et al. KOOLS-IFU: Kyoto Okayama Optical Low-dispersion Spectrograph with optical-fiber Integral Field Unit. *Publ. Astron. Soc. Jpn*, **71**, 102 (2019).

39. Ozaki, S. & Tokimasa, N. The optical spectrograph for the NAYUTA telescope I. Design. *Annual Report of the Nishi-Harima Astronomical Observatory (ISSN 0917-6926)*, **15**, 15-29 (2005)
40. Namekata, K. et al. Optical and X-ray observations of stellar flares on an active M dwarf AD Leonis with the Seimei Telescope, SCAT, NICER, and OISTER. *Publ. Astron. Soc. Jpn*, **72**, 68, (2020).
41. Gaia Collaboration et al. Gaia Data Release 2. Summary of the contents and survey properties. *Astron. Astrophys.*, **616**, A1, (2018)
42. Seki, D. et al., SMART/SDDI Filament Disappearance Catalogue. *Sun and Geosphere* **14**, 95, (2019)
43. Jain, R. & Sorathia, B. Flare-associated surge prominence on 1980 October 30. *Astron. Astrophys.*, **8**, 295 (1987).
44. Liu, Y. & Kurokawa, H. On a Surge: Properties of an Emerging Flux Region. *Astrophys. J*, **610**, 1136 (2004).
45. Ohyama, M. & Shibata, K. X-ray Plasma Ejection Associated with H α Filament Eruption. *Solar Physics with Radio Observations, Proceedings of the Nobeyama Symposium*, **479**, 367-370 (1998).
46. Christian, D. J. et al., H α and EUV Observations of a Partial CME. *Astrophys. J*, **804**, 147 (2015).

47. Emslie, A. G. et al., Global Energetics of Thirty-eight Large Solar Eruptive Events. *Astrophys. J.*, **759**, 71 (2012).
48. Sakaue, T. et al. Observational study on the fine structure and dynamics of a solar jet. II. Energy release process revealed by spectral analysis. *Publ. Astron. Soc. Jpn.*, **70**, 99, (2018)
49. Mein, P. & Mein, N. Differential cloud models for solar velocity field measurements. *Astron. Astrophys.*, **203**, 162, (1988)
50. Odert, P. et al., Stellar coronal mass ejections - II. Constraints from spectroscopic observations. *Mon. Not. R. Astron. Soc.*, **494**, 3766 (2020).
51. Tsiropoula, G. & Schmieder, B. Determination of physical parameters in dark mottles. *Astron. Astrophys.*, **324**, 1183 (1997).
52. Flores Soriano, M. & Strassmeier, K. G., Short-term evolution and coexistence of spots, plages and flare activity on LQ Hydrae. *Astron. Astrophys.*, **597**, A101 (2017)
53. Vida, K., et al., The quest for stellar coronal mass ejections in late-type stars. I. Investigating Balmer-line asymmetries of single stars in Virtual Observatory data. *Astron. Astrophys.*, **623**, A49 (2019)
54. Gunn, A. G. et al., High-velocity evaporation during a flare on AT Microscopii. *Astron. Astrophys.*, **285**, 489 (1994).
55. Fuhrmeister, B. & Schmitt, J. H. M. M. Detection and high-resolution spectroscopy of a huge flare on the old M 9 dwarf DENIS 104814.7-395606.1. *Astron. Astrophys.*, **420**, 1079 (2004).

56. Fuhrmeister, B., et al., Multiwavelength observations of a giant flare on CN Leonis. I. The chromosphere as seen in the optical spectra. *Astron. Astrophys.*, **487**, 293, (2008)
57. Leitzinger, M. et al., A search for flares and mass ejections on young late-type stars in the open cluster Blanco-1. *Mon. Not. R. Astron. Soc.* **443**, 898-910 (2014).
58. Korhonen, H. et al., Hunting for Stellar Coronal Mass Ejections. *Living Around Active Stars, Proceedings of the International Astronomical Union, IAU Symposium* **328**, 198-203 (2017).
59. Muheki, P. et al., Properties of flares and CMEs on EV Lac: possible erupting filament. *Mon. Not. R. Astron. Soc.* **499**, 5047-5058 (2020)
60. Maehara, H., et al., Time-resolved spectroscopy and photometry of M dwarf flare star YZ Canis Minoris with OISTER and TESS: Blue asymmetry in the H α line during the non-white light flare. *Publ. Astron. Soc. Jpn.* **73**, 44 (2021)
61. Zic, A., et al., A Flare-type IV Burst Event from Proxima Centauri and Implications for Space Weather. *Astrophys. J.*, **905**, 23 (2020)
62. Guenther, E. W., Emerson, J. P., Spectrophotometry of flares and short time scale variations in weak line, and classical T Tauri stars in Chamaeleon. *Astron. Astrophys.* **321**, 803-810 (1997).
63. Haisch, B. M., et al., Coordinated Einstein and IUE observations of a disaritions brusques type flare event and quiescent emission from Proxima Centauri. *Astrophys. J.*, **267**, 280 (1983)
64. Ottmann, R. & Schmitt, J. H. M. M., ROSAT observation of a giant X-ray flare on Algol: evidence for abundance variations? *Astron. Astrophys.*, **307**, 813 (1996)

65. Wheatley, P. J., ROSAT observations of V471 Tauri, showing that stellar activity is determined by rotation, not age. *Mon. Not. R. Astron. Soc.*, **297**, 1145 (1998)
66. Tsuboi, Y. et al., ASCA Detection of a Superhot 100 Million K X-Ray Flare on the Weak-Lined T Tauri Star V773 Tauri. *Astrophys. J.*, **503**, 894 (1998).
67. Favata, F. & Schmitt, J. H. M. M. Spectroscopic analysis of a super-hot giant flare observed on Algol by BeppoSAX on 30 August 1997. *Astron. Astrophys.*, **350**, 900 (1999).
68. Franciosini, E., et al., BeppoSAX observation of a large long-duration X-ray flare from UX Arietis. *Astron. Astrophys.*, **375**, 196 (2001)
69. Pandey, J. C. & Singh, K. P., A study of X-ray flares - II. RS CVn-type binaries. *Mon. Not. R. Astron. Soc.*, **419**, 1219 (2012)
70. Ambruster, C. W., et al., An episode of mass expulsion from the M-dwarf flare star EV Latertae ? *New Insights in Astrophysics*, **263**, 137 (1986)
71. Bond, H. E., et al., Hubble Space Telescope Imaging of the Outburst Site of M31 RV. II. No Blue Remnant in Quiescence. *Astrophys. J.*, **560**, 919 (2001)
72. Parsons, S. G., et al., Eclipsing post-common envelope binaries from the Catalina surveys. *Mon. Not. R. Astron. Soc.*, **429**, 256 (2013)
73. Leitzinger, M., et al., A census of coronal mass ejections on solar-like stars. *Mon. Not. R. Astron. Soc.*, **493**, 4570 (2020)

74. Leitzinger, M., et al., Stellar activity at FUV/Radio wavelengths. *Central European Astrophysical Bulletin*, **34**, 123 (2010)
75. Boiko, A. I., et al., Search of the radio emission from flare stars at decameter wavelengths. *Advances in Astronomy and Space Physics*, **2**, 121 (2012)
76. Villadsen, J., Hallinan, G., & Bourke, S., Radio spectroscopy of stellar flares: magnetic reconnection & CME shocks in stellar coronae. *Solar and Stellar Flares and their Effects on Planets*, **320**, 191 (2016)
77. Crosley, M. K., et al., The Search for Signatures of Transient Mass Loss in Active Stars. *Astrophys. J.*, **830**, 24 (2016)
78. Crosley, M. K. & Osten, R. A., Constraining Stellar Coronal Mass Ejections through Multi-wavelength Analysis of the Active M Dwarf EQ Peg. *Astrophys. J.*, **862**, 113 (2018)
79. Crosley, M. K. & Osten, R. A., Low-frequency Radio Transients on the Active M-dwarf EQ Peg and the Search for Coronal Mass Ejections. *Astrophys. J.*, **856**, 39 (2018)
80. Villadsen, J. & Hallinan, G. , et al., Ultra-wideband Detection of 22 Coherent Radio Bursts on M Dwarfs, *Astrophys. J.*, **871**, 214 (2019)
81. Allred, J. C. et al., Radiative Hydrodynamic Models of the Optical and Ultraviolet Emission from Solar Flares. *Astrophys. J.*, **630**, 573 (2005).
82. Tei, A., Sakaue, T., Okamoto, T. J., et al., Blue-wing enhancement of the chromospheric Mg II h and k lines in a solar flare. *Publ. Astron. Soc. Jpn.* **70**, 100, (2018)

83. Kuridze, D., Mathioudakis, M., Simões, P. J. A., et al., H α Line Profile Asymmetries and the Chromospheric Flare Velocity Field *Astrophys. J.*, **813**, 125, (2015)
84. Heinzel, P., Karlicky, M., Kotrc, P., et al., On the Occurrence of Blue Asymmetry in Chromospheric Flare Spectra. *Solar Physics*, **152**, 393, (1994)
85. Schwartz, P. et al., Prominence Visibility in Hinode/XRT Images. *Astrophys. J.*, **807**, 97 (2015).
86. Osten, R. A. & Wolk, S. J. A Framework for Finding and Interpreting Stellar CMEs. *Living Around Active Stars, Proceedings of the International Astronomical Union, IAU Symposium*, **328**, 243-251 (2017).
87. Giampapa, M. S., et al., A preflare diminution in the quiescent flux of EQ Pegasi. *Astrophys. J. L.*, **252**, L39 (1982)
88. Doyle, J. G. & Collier Cameron, A., Mass ejections from the rapidly rotating M dwarf star GL 890. *Mon. Not. R. Astron. Soc.*, **244**, 291 (1990)
89. Airapetian, V. S. et al., Prebiotic chemistry and atmospheric warming of early Earth by an active young Sun. *Nat. Geosci.* **9**, 452-455 (2016).